Evaluation of hybrid strong flange I-sections under compression

Gregory Langone [a*], Usman Ali [b*], Barbara Rossi [a b]
[a] University of Oxford, England; gregory.langone@new.ox.ac.uk, barbara.rossi@new.ox.ac.uk.
[b] KU Leuven, Belgium; usman.ali@kuleuven.be, barbara.rossi@kuleuven.be.
[*] Co-first authors.

Abstract

Hybrid I-sections are frequently designed with slender webs and thick flanges, and greater material strength in the flanges. Under the fundamental load case of pure compression or bending, a compressed flange will approach fully plastic capacity before failure, while the web develops only its local buckling capacity, a long-overlooked failure mechanism not currently integrated into design-ready tools. This paper provides the first systematic experimental and numerical assessment of the effect of hybridity on strong flange sections, establishing the experimentally grounded and numerically validated basis required to quantify this behaviour and incorporate it into design-oriented strength models. We present the test method, results, and analysis of thirteen stub column tests on hybrid stainless steel I-profiles, exhibiting strong flange behaviour. The tested sections are comprised of web and flange plates made from a combination of austenitic and duplex stainless steels and carbon steel, fabricated by TIG welding. Tensile coupon tests are conducted on each constituent plate to measure material properties. Geometric imperfections for the web and flanges of each column are measured by pairing an adapted CNC machine with a linear variable differential transformer. The stub columns are compressed under a constant displacement rate while strains are measured at multiple locations using a video extensometer alongside digital image correlation. A finite element model of the compression tests is developed in Abaqus and validated against the experimental results. The influence of individual geometrical and material properties on buckling mechanisms and ultimate strength is analysed. The experimental results in this paper provide the essential foundations to then develop a new

Submitted Copy

DSM formulation that explicitly captures the governing behaviour of hybrid strong flange I-sections, addressing a key gap in current design practice.

1. Introduction

Hybrid steel members – made up of two or more plates of different steel grades welded together – provide the possibility to select material properties that best meet the demands on each member element. Properly designed hybrid members can have highly desirable performance characteristics, including greater ultimate strength and the ability to influence local buckling and ductility characteristics [1].

Hybrid carbon steel members have existed in construction practice for over 50 years and have been rather extensively studied. In this time, they have been employed predominantly in bridges as I-profile girders subjected to compression and/or bending – with stronger material in the flanges to resist the high stresses furthest from the neutral bending axis. Today's body of research from over 120 publications on hybrid girders under flexure is well summarized by Terreros-Bedoya et al. in [2].

Provisions which accommodate the design of hybrid members are still rare in current design codes and tend to exclusively focus on carbon steel hybrid girders under flexure. This is, at least in part, driven by a shortage of experimental evidence needed to validate numerical models and assess the applicability of design methods. The AASHTO Bridge Design Specification [3] and EN 1993-1-5 [4] each contain rules for the design of hybrid girders. These codes give different guidelines for the allowable hybrid ratio i.e. yield strength of the flanges divided by that of the web ($f_{y,f} / f_{y,w}$). AASHTO requires web elements to have a yield strength of at least 70% of the flange yield strength or 250MPa, whichever is greater [3]. This limit was developed based on research by Frost in the 1960's [5], an ASCE experimental report [6], and I-girder tests by Mozer et al. [7]. Conversely, the Eurocode

Submitted Copy

recommends a hybrid ratio ≤2.0, and states that the value of the material coefficient ε, defined in EN 1993-1-5 as a function of f_y, to calculate effective area of the web must be based on the yield strength of the compression flange. This standard was developed based on an additional 35 years of experimental evidence and design recommendations provided by Veljkovic & Johansson [8]. The recent publication by Terreros-Bedoya et al. [2] concludes that the optimal and safe hybrid ratio for flexural members ranges between 1.3 and 1.6.

Noteworthy, compression resistance is fundamental and the worst-case loading condition to understand before addressing flexure [9]. However, the cumulative body of research on hybrid steel members under compression, as summarized in Table 1, is limited and concentrates on rather complex cross-sectional shapes. The dividing lines in Table 1 demarcate groups of directly related papers.

Table 1. Literature addressing the behaviour of hybrid steel sections under compression.

Author	Year	Evidence Type	Shape
NagarajaRao et al. [10]	1969	Test	I-section
NagarajaRao et al. [11]	1972	Test	I-section
Zhao et al. [12]	2004	Test	Bespoke
Binh et al. [13]	2004	Numerical	Bespoke
Rhodes et al. [14]	2005	Test	Bespoke
Javidian et al. [1]	2016	Test + Numerical	Bespoke
Farmani et al. [15]*	2023	Test + Numerical	Bespoke
Lalthazuala & Singh [16]*	2020	Numerical	I-section
Liu et al. [9]	2022	Test + Numerical	T-shape
Liu et al. [17]	2022	Test + Numerical	T-shape
Chen et al. [18]	2023	Test	I-section
Chen et al. [19]	2023	Numerical	I-section
Bock et al. [20]*	2023	Numerical	I-section

* includes stainless steel elements or members.

Hybrid steel members under compression were first investigated in 1965 and 1969 by NagarajaRao et al. [10, 21]. With theoretical and experimental evidence, they concluded that hybrid columns could be more cost efficient than their homogeneous counterparts within a certain slenderness range [11]. Following those tests, hybrid columns were not investigated

Submitted Copy

for a period of 30 years until Zhao et al. [12] re-opened the topic to assess whether a hybrid design could be used to produce structurally efficient high-capacity columns. The authors studied a complex, bespoke design for hollow square and triangular columns (based on Aoki & Ji [22]) – placing ultra-high strength circular tubes on the corners (f_y=1350 MPa) welded to mild steel plates on the sides (f_y=350 MPa). Binh et al. developed a finite element (FE) model corresponding to Zhao et al.'s experimental specimens [13], and Rhodes et al. proposed the corresponding design analysis procedure [14]. The conclusive paper by Javidan et al. [1] showed that this hybrid design combining hollow sections and plates improved both the ultimate strength and ductility characteristics. Farmani et al. investigated similar tube/plate structures focusing on the fire resistance of UHSS (ultra-high-strength steel, >1200 MPa) tubes welded to plates of austenitic stainless steel [23], then analysed the effects of fire on the hybrid columns proposed by Zhao et al. [15]. Although incredibly interesting and promising, this series of papers focusses exclusively on the specific bespoke design and does not explore the potential of more practical hybrid concepts, suitable for mainstream structural engineering applications such as I-profiles. Nevertheless, the tests by Zhao et al. and the subsequent related investigations made clear that design guidelines and behavioural descriptions developed for hybrid sections needed improvements, particularly for pure compression. Importantly, the studied sections included materials with yield strength differences of approximately 3 times. This is far outside the range allowed by codes [12, 1], and much greater than the optimal ratio of 1.3-1.6 recommended by Terreros-Bedoya et al. [2] for flexural members. This disparity provides standing to assume that the optimal ratio is likely to be very different for hybrid members under compression.

In 2022, local buckling of hybrid HSS (high strength steel, *>460 MPa*) columns was studied by Liu et al. who conducted experiments on T-section stub columns with HSS in the web and assessed the applicability of three design methods [9]. They found that the Direct

Submitted Copy

Strength Method (DSM) provided accurate yet conservative predictions while the Continuous Strength Method (CSM) was conservative for slender sections. Later, in 2023, Chen et al. published three studies on hybrid I-profile columns. The first study described welding effects on hybrid sections and proposed a new residual stress distribution model [24]. The second reported experiments on twelve hybrid I-section columns [18] and described a FE model which was validated against the tests. Third, in [19], a parametric assessment focused on local buckling behaviour and confirmed that the critical plate element – defined as the plate with the lowest elastic local buckling stress – governed local buckling behaviour and that interaction between web and flange plates was significant in the studied body of hybrid I-sections. Among these studies, most of the existing experimental evidence on hybrid sections in compression revolves around HSS – particularly for increasing the ductility of sections with HSS and assessing the applicability of design methods to these materials.

Despite initial costs approximately four times greater than carbon steel alternatives, stainless steel presents the advantage of excellent corrosion resistance, which can lead to lower lifecycle impacts (both financial and in CO_2 emissions accounting) compared to carbon steel equivalents [25, 26, 27]. The non-linear stress-strain properties of stainless steels affect their buckling behaviour [28]. For this reason, stainless steel I-sections were tested in compression by Yuan et al. focusing on local-overall interaction buckling [29] and Gardner et al. & Ran et al. focusing on laser welded sections [30, 31]. These studies, however, do not cover the behaviour of hybrid stainless steel members which, due to their non-linear material properties, must be considered separately from the behaviour of hybrid carbon steel. Two recent studies do focus on hybrid stainless steel sections in compression or in bending, however, neither presents experimental evidence. Bock et al. numerically modelled hybrid stainless steel sections in compression and bending and extended the CSM to the design of hybrid austenitic and duplex girders [20]. Lalthazuala and Singh proposed a new form of the

Submitted Copy

DSM for hybrid stainless steel columns based on a numerical study [16], however the proposed modification focused only on design accuracy in the low slenderness range.

Last, of all the papers mentioned in this state-of-the-art, none specifically focusses on the compression behaviour of I-profiles characterised by strong flange behaviour; this is a distinct behaviour identified by Rossi & Li in 2013 – discussed further in Section 1.2 – based on FE models of over 1,450 hot-rolled carbon steel I-profile stub columns [32]. Because most hybrid I-sections are designed with thick flanges made of the stronger material compared to the web, these sections can exhibit unique behaviour termed “strong flange” when the difference in plate strengths is large [33, 32], as is explained further in Section 1.2.

Our paper reports the findings from thirteen stub column compression tests on fabricated (sometimes referred to as “built-up”) I-profiles. Among these columns are ten hybrid sections – eight made of stainless steel and two made of stainless steel and carbon steel, the first experimental evidence for these categories – and three homogeneous stainless steel sections. Strong flange behaviour is identified as effecting all tested columns. The local buckling behaviour of each column during the test is studied and their ultimate strengths are reported. The test results are compared to the strength and failure mechanism from a FE model of each column to study the influence of individual parameters on column behaviour. This paper establishes a robust modelling framework suitable for parametric and design-oriented studies, forming the groundwork for the development of a new Direct Strength Method formulation for hybrid strong flange I-sections developed in [34]. The experimental and numerical work in this paper, followed by the design recommendations developed in [34], detail a comprehensive approach to studying the long overlooked failure mode of strong flange behaviour and provides the evidence to understand broader combinations of materials and geometries in hybrid sections.

1.2. Strong Flange Behaviour

Submitted copy

In 2010, Seif & Schafer's study on the local buckling of standard hot-rolled steel I-sections found that the web critical buckling stress was strongly correlated with a ratio of the profile geometric dimensions [35], namely *LD* for "limiting dimension" defined in *Eq. 1b*. A regression was fit to empirically determine the relationship between *LD* and the web buckling coefficient k_w, *Eq. 1a*. However, the relationship quantified by *Eq. 1a* is only applicable to the range of I-profile sections included in Seif & Schafer's study. Bryan's buckling formula (*Eq. 2*) [36] could then be used to estimate the critical buckling stress of the web plate – which now accounts for the geometry of the web and its flange restraints.

$$\frac{1}{k_w}=\frac{1.5}{\left(\left(\frac{h_c}{t_w}\right)\left(\frac{2t_f}{b}\right)\right)^{2.5}}+0.18 \tag{1a}$$

$$1.80 \le LD \le 10.94 \text{ with } LD=\left(\frac{h_c}{t_w}\right)\left(\frac{2t_f}{b}\right) \tag{1b}$$

where h_c is the height of the section measured between the centre of the flanges.

$$\sigma_{crl}=k_w\frac{\pi^2 E}{12(1-\mu^2)}\left(\frac{t}{b}\right)^2 \tag{2}$$

Since hybrid I-sections typically use thick flanges made from the higher-strength material, they can display pronounced strong flange behaviour [33, 32]. This behaviour was first described in 2013 by Rossi & Li who used the FE method to simulate the behaviour of over 1,450 hot-rolled carbon steel I-profiles in pure compression [32]. They detected a clear difference in ultimate strength depending on whether the limiting dimension was above or below Seif & Schafer's threshold of 10.94.

Rossi and Li observed that sections with $LD>10.94$ exhibited local buckling of the web and very minimal deflection of the flanges, elucidating the boundary of Seif & Schafer's *Eq. 5a*. They posited that the flange was developing (or approaching) fully plastic capacity before failure, while the web developed only its local buckling capacity i.e. 'strong flange

Submitted copy

behaviour'. *Eq.* 3 was proposed in [32] to predict the ultimate strength of sections with $LD>10.94$, where *Eq. 2* was used to calculate the elastic critical local buckling stress. In cases where $LD<10.94$, the traditional codified DSM was applied. This method performed well for predicting the strength of the numerically modelled sections, but there was little experimental evidence available at the time to evaluate the method further.

$$P_{nl}=\left(2b_f t_f f_{y,f}\right)+\left(h_w t_w \sigma_{crl,w}\right) \tag{3}$$

While Rossi & Li's method describes the behaviour of strong flange I-profiles, the use of the limiting dimension does not account for the possibility of different materials in the web and flange. A method applicable to hybrid sections should independently incorporate the yield strength in both the web and the flange to account for their effects on plate slenderness and interactions between the plates. In 2024, Langone et al. demonstrated that the slenderness ratio Ω given in *Eq. 4* – which is the plate slenderness of the web divided by the plate slenderness of the flange – could more accurately categorize strong flange behaviour while incorporating the different material strengths in hybrid sections [33]. The *LD* and Ωequations are very similar – which is expected as they aim to capture the same behaviour.

$$\Omega=\left(\frac{h_w}{t_w}\sqrt{f_{y,f}}\right)/\left(\frac{\left(b_f-t_w\right)}{2t_f}\sqrt{f_{y,w}}\right) \tag{4}$$

$$\kappa'=\frac{2t_f b_f f_{y,f}}{t_w h_w \sigma_{crl}} \tag{5}$$

$$if\ \lambda_l>0.776\begin{cases} P_{nl}=\left[1-0.15\left(\frac{P_{crl}}{P_{ne}}\right)^{0.4}\right]\left(\frac{Pcrl}{P_{ne}}\right)^{0.4}P_{ne}\ if\ \Omega\le 11.17 \\ P_{nl}=\left[\frac{1}{1-0.0208\kappa'}\right]\left[1-0.15\left(\frac{P_{crl}}{P_{ne}}\right)^{0.4}\right]\left(\frac{Pcrl}{P_{ne}}\right)^{0.4}P_{ne}\ if\ \Omega>11.17 \end{cases} \tag{6}$$

Submitted Copy

Langone et al. then developed the strength ratio κ' shown in *Eq. 5*, which is based on Rossi & Li's hypothesis that strong flange sections will develop critical buckling strength in the web and fully plastic resistance in the flanges. By positing that as the ratio of flange-to-web capacity increases, the extent of deviation from existing design predictions also increases, they incorporated the strength ratio to generate a modified equation for the DSM, see *Eq. 6*. A coefficient of 0.0208 was originally proposed by Langone et al. to accompany the κ' parameter, and a threshold of 11.17 was set for Ω. These values were based on the preliminary numerical evidence of strong flange hot-rolled carbon steel I-sections presented in [32]. Proper evidence to assess this method – including strong flange, hybrid, and built-up members – was not available until the tests and FE model presented in this paper. Ultimately, *Eq. 6* proposed in [33] is proven insufficiently accurate by the test and FE model evidence. However, the premise of the slenderness ratio and strength ratio being incorporated into the DSM equation proved an invaluable conceptual leap leading to the design proposal given in [34].

1.3. Impact and Efficiency Gains

The principal advantage of hybrid and strong flange I-sections is the potential for increased structural efficiency, making them particularly attractive for large, fabricated compression members in high-rise or high-span buildings, where efficiency demands are high. When columns are required to resist high levels of axial force combined with flexure, the I-profile geometry, with its deep web, offers efficient combined flexural and axial resistance alongside practical advantages for connection detailing. Hybrid and strong flange members are inherently more complex to design than their homogenous counterparts. For this reason, these sections are more likely to be adopted in projects where the increased design cost can be offset by meaningful reductions in material usage and construction costs. Examples of applications of hybrid sections include lower-story columns in high-rise

Submitted Copy

buildings, as studied by Zhao et al. [12]. Structural efficiency gains in these types of projects can be realized based on the experimental evidence provided in this paper, and the development of improved design method in [34].

2. Design and Fabrication

Thirteen stub columns were designed to investigate the effects of specific material properties and geometries on local buckling behaviour and ultimate strength. The stub columns include stainless steel grades 1.4307, 1.4462, and 1.4404 and carbon steel grade S275. This study focuses on two geometric parameters affecting local buckling and ultimate strength: the height of the web and the ratio between the web and flange thickness, being either 0.5 or 1.0. The stub columns were therefore designed by varying these parameters alongside the grades of carbon or stainless steel used. The FE method was used to compute the nominal ultimate strength of each section as a check prior to fabrication. The nominal length of the columns was selected to ensure local web buckling would fully develop in each specimen. This was also checked via FE modelling prior to testing.

A diagram of the section dimensions is given in Figure 1a and geometric imperfections labels are described in Figure 1b. The complete nominal dimensions and materials for each specimen are reported in Table 2, while measured values are reported in Table 3. The measured stress-strain curves of all materials are reported in Section 3.

The stub columns were designed to cover a slenderness range from 0.75 to 2.96, which includes sections theoretically reaching full cross-section plasticity and sections exhibiting strong flange behaviour. In Table 2, the columns are separated into three categories indicated by thin dividing lines. The top category is hybrid sections with different plate thicknesses in the web and flange, the middle category is hybrid sections with equal plate thicknesses, and the bottom category is homogeneous sections with different plate thicknesses. The thirteen

Submitted Copy

stub columns are designed to demonstrate the effect of incremental changes on multiple material and geometric parameters. The following naming convention was developed to track parameters changing between the columns (e.g., changed web height, flange width, flange thickness or the change from austenitic to duplex grades of stainless steel): Columns are given an alphanumeric identifier with each number indicating a specific combination of materials in the web and flange, and each letter indicating a specific set of cross-section geometries. Therefore, any two columns labelled with the same letter can be compared on the basis that their only difference is material properties. Likewise, any two columns with the same number are compared knowing that their only difference is geometry.

For example, the comparison between D1 and D3 isolates a change in the web material from grade 1.4307 austenitic stainless steel to 1.4404 duplex. Similarly, the comparison between C1 and D1 isolates a change in the web height, while all other properties are held constant. The resulting differences in ultimate strength, deformation shape, and the force-displacement curve are discussed in Section 6.

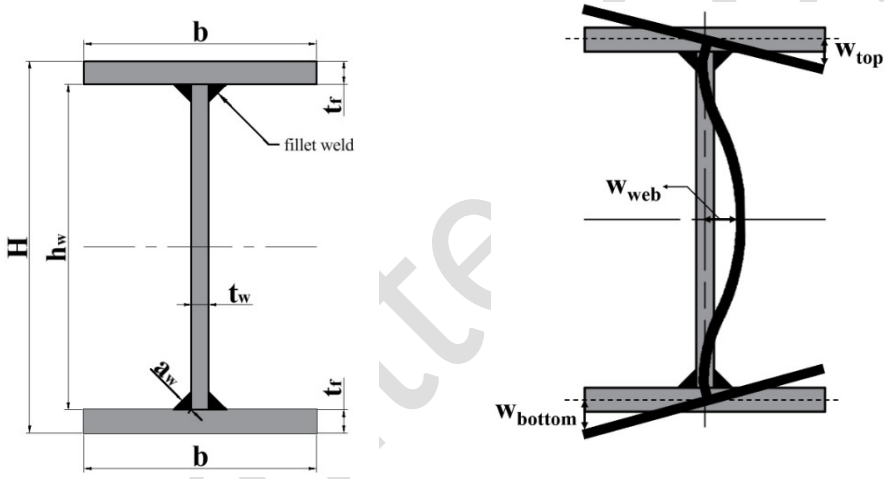
Table 2. Nominal geometrical dimensions and materials for stub column specimens.

Specimen	L [mm]	h_w [mm]	b [mm]	t_w [mm]	t_f [mm]	t_w / t_f	Flange Grade	Web Grade
A1	350	200	60	3	6	0.5	1.4462	1.4307
B1	350	88	60	3	6	0.5	1.4462	1.4307
A2	350	200	60	3	6	0.5	1.4462	S275
B2	350	88	60	3	6	0.5	1.4462	S275
C1	350	394	80	3	3	1.0	1.4462	1.4307
D1	350	325	80	3	3	1.0	1.4462	1.4307
E1	350	94	60	3	3	1.0	1.4462	1.4307
C3	350	394	80	3	3	1.0	1.4462	1.4404
D3	350	325	80	3	3	1.0	1.4462	1.4404
E3	350	94	60	3	3	1.0	1.4462	1.4404
F3	350	300	90	3	6	0.5	1.4307	1.4307
G3	350	288	90	3	6	0.5	1.4307	1.4307
F4	350	300	90	3	6	0.5	1.4404	1.4404

Table 3. Measured dimensions and material strengths for stub column specimens.

Submitted Copy

Specimen	L [mm]	h_w [mm]	b [mm]	t_w [mm]	t_f [mm]	a_w [mm]	Flange $\sigma_{0.2}$ [MPa]	Web $\sigma_{0.2}$ [MPa]
A1	349.3	198.3	59.39	3.02	6.46	2.4	613.0	282.5
B1	349.2	87.3	59.70	2.96	6.45	1.8	613.0	282.5
A2	349.2	198.1	59.58	2.96	6.44	1.8	613.0	336.6
B2	348.8	87.1	59.86	2.96	6.47	2.4	613.0	336.6
C1	349.0	393.2	78.94	2.95	3.01	1.8	617.3	282.5
D1	348.8	323.9	78.49	2.98	3.06	2.4	617.3	282.5
E1	348.8	92.2	59.50	2.96	3.01	1.8	617.3	282.5
C3	349.2	392.7	79.13	2.99	3.01	2.4	617.3	269.6
D3	349.2	323.7	78.42	3.01	3.02	2.4	617.3	269.6
E3	348.3	92.7	59.29	3.02	3.01	1.8	617.3	269.6
F3	349.2	298.4	88.91	2.97	6.06	2.4	331.7	282.5
G3	349.3	285.2	89.39	2.95	6.03	2.4	331.7	282.5
F4	343.0	298.1	89.23	3.02	6.08	2.4	359.0	269.6



(a) *(b)*

Figure 1. Diagram of I-profile *(a)* geometric dimensions and *(b)* imperfections.

Plates were cut by waterjet to the nominal dimensions. Gas tungsten arc welding (GTAW), also called tungsten inert gas (TIG) welding, was used to fabricate the stub columns. Inevitable distortions were induced during the welding process, and their effects on the stub column stability is addressed in Section 4 on geometric imperfections and in Section 6.3 on numerical model parameters. The column ends were milled parallel to each other to provide uniform flat surfaces to contact the compression platens. Column ends were then treated with a belt sander to further improve contact uniformity. Any remaining gaps in the column-platen contact were measured prior to each test and ensured to be less than 1 mm.

Submitted

3. Material Properties

Tensile coupons were tested for material grades and thicknesses corresponding to those used in the stub column constituent plate elements. All coupons were cut in the longitudinal direction relative to the direction of rolling. Before testing, the dimensions of each coupon were measured at multiple locations and the average dimensions were recorded. Mill certificates were provided for each material, including the chemical compositions and the average measured properties of $R_{p0.2}$ and R_m which are included in Table 4. The tensile tests were conducted in accordance with ISO-6892-1-2019 [37] using an Instron 8804MT press. The force was recorded directly by the Instron press. The Instron 2nd generation Advanced Video Extensometer (AVE2) – with measurement accuracy of ±0.5% – measured tensile strain by tracking the distance between two points on opposite ends of the coupon gauge width. Expectedly, the video extensometer (VE) measurement was more accurate than the displacement readings from the press, particularly during initial loading, since machine compliance is excluded from these readings.

Table 4. Measured material properties from tensile coupons.

Grade	Thickness [mm]	Measured				Code Specified			Mill Certificate	
		E [GPa]	**$\sigma_{0.2}$** [MPa]	**σ_u** [MPa]	**ε_f** [mm/mm]	**E** [GPa]	**$\sigma_{0.2}$** [MPa]	**σ_u** [MPa]	**$R_{p0.2}$** [MPa]	**R_m** [MPa]
1.4462	6.52	201.3	613.0	776.1	0.311	200	500	700	638	802
1.4462	2.99	202.3	617.3	825.7	0.304	200	500	700	631	844
1.4307	5.98	202.3	331.7	642.2	0.639	200	220	520	355	630
1.4307	2.93	194.2	282.5	663.6	0.684	200	220	520	291	622
1.4404	5.96	197.1	359.0	594.3	0.603	200	240	530	350	595
1.4404	2.99	*	269.6	622.5	0.610	200	240	530	307	602
S275	2.90	192.7	336.6	468.4	0.159	210	275	430	361	488

*The video extensometer did not accurately read the initial stiffness or elasticity for the 1.4404 3mm coupon. The measured value for the Young's Modulus was 159.5 GPa. The more accurate value of 197.1 GPa, measured in the 1.4404 6mm coupon, was therefore used to calculate the 0.2% proof stress and in the FE material model.

The material properties for Young's Modulus E , 0.2% proof stress $\sigma_{0.2}$, ultimate tensile stress σ_u, and the strain at failure ε_f were determined from the tensile test results for the plates

Submitted Copy

included in the stub columns tested in this paper and reported in Table 4. The Young's modulus is calculated as the slope of a linear regression on the stress-strain relationship within initial domain where this relationship is linear. The strain value where this relationship departs from linearity is different in each coupon, but generally occurs between 0.0005 to 0.002 mm/mm. The 0.2% proof stress is calculated by plotting a line with the *x*-intercept as 0.002 mm/mm and the slope as the measured Young's Modulus. The stress value where this line intersects the measured stress-strain curve is the 0.2% proof stress. Ultimate tensile stress is taken as the greatest stress value measured during the test up to fracture. Figure 2 shows the stress-strain curve from the VE measurement for all nine tensile coupons, with the curves ending at the point of fracture or where the coupon failed to provide any further tensile resistance.

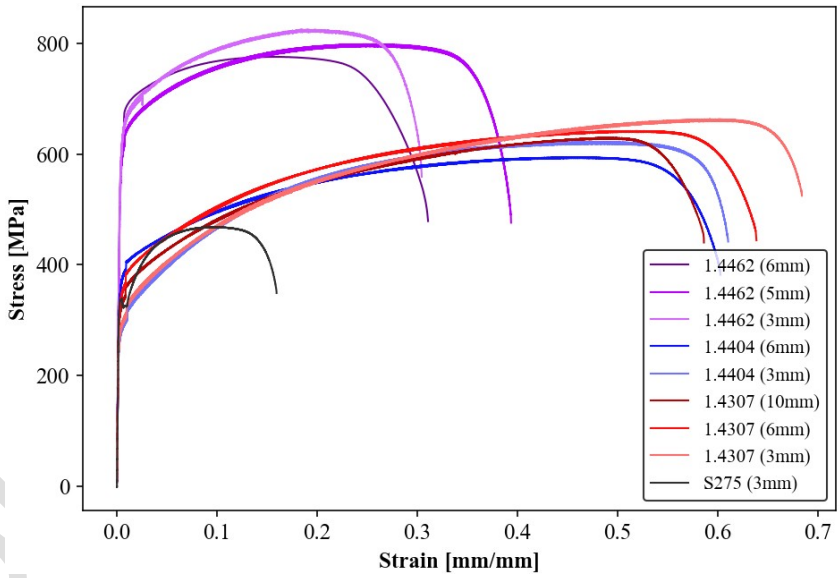


Figure 2. Stress-strain curves from eight tensile coupon tests.

4. Initial Geometric Imperfections

Precise measurements were taken to observe the shape and magnitude of the imperfections in the web and flanges for all specimens. Imperfections organic to the plates are induced by uneven cooling after hot-rolling. The greatest share of the cross-sectional imperfections, however, is the result of distortions occurring due to welding. Figure 1b

depicts how the maximum imperfection amplitudes are defined on each plate. A measurement procedure was developed to capture the geometric imperfections of the stub columns at relatively low cost. The measurement setup for web imperfections is shown in Figure 3.

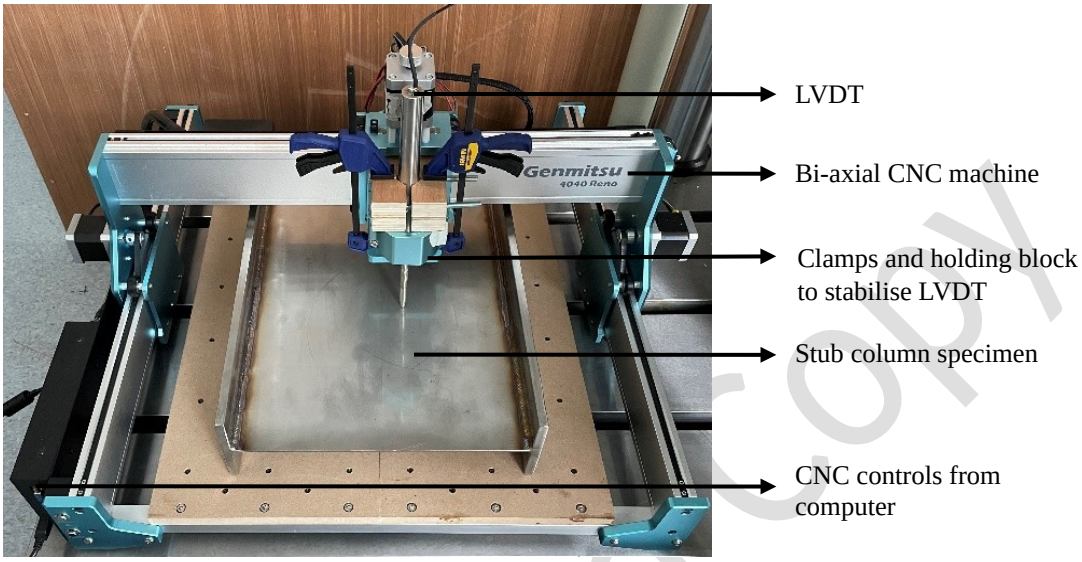


Figure 3. Measurement set-up for geometric imperfections of the web.

A Genmitsu 4040 Reno CNC machine was operated from a laptop with G-code commands. The LVDT accessory for the Instron 8804MT press was attached to the CNC machine, which was programmed to trace five evenly spaced parallel lines, each the length of the column, to survey the three plates composing each column. Displacement measurements were taken from the LVDT at a rate of 20Hz and recorded through the Instron Console. The accuracy of the CNC machine's position was controlled within ±0.1mm. Based on time readings, the displacement measurements were associated with (x, y, z) coordinates covering the web and flange plates. A mesh was interpolated between the five discrete rows traced along the length of each plate using the SciPy package in python. The resulting surface visualization of the web imperfection shapes and amplitudes is provided in Figure 4.

Submitted Copy

The out-of-plane deformations are shown by the colour scales in Figure 4, given in millimetres. Two scales are provided to best visualize the shape of all sections given some have much larger imperfection amplitudes than others. In sections with large web height, a single half-wave shape is generally identified. In sections where the web height is too short for a full half-wave to develop (B1, B2, E1, and E3), there is less consistency in the imperfection shape and the imperfection magnitude tends to be smaller. The maximum measured geometric imperfection for each plate is reported in Table 5.

The measured imperfection amplitudes are also compared against the recommended magnitudes for FE modelling given in EN 1993-1-5. The Eurocode recommended magnitude for the critical (web) plate is provided for reference in Table 5, i.e. the minimum of (a, b)/200 where a is the distance between transverse stiffeners (here the member length, since it is unstiffened) and b is the plate width [4]. Sections for which the measured imperfection magnitude exceeds the Eurocode modelling recommendation are marked with an asterisk in Table 5. All flange plates exceeded the EN 1993-1-5 recommendation – which is unsurprising as our samples are individually welded (rather than hot rolled or mass-produced) and have narrow flanges. Additionally, the Eurocode guidelines were not established for hybrid sections made of different materials, or for materials where lower thermal conductivity (e.g. stainless steel) can cause welding distortions [38].

Table 5. Measured maximum geometric imperfection magnitude on each plate.

Specimen	$w_{\text{top flange}}$ [mm]	$w_{\text{bottom flange}}$ [mm]	w_{web} [mm]	EN 1993-1-5 (a, b)/200 web [mm]
A1	1.50	1.68	0.40	0.99
B1*	1.26	1.81	0.76	0.44
A2	1.67	1.32	0.39	0.99
B2*	1.57	1.55	2.66	0.44
C1	1.81	0.95	0.91	1.75
D1	1.57	1.02	1.08	1.62
E1	0.57	0.44	0.37	0.46
C3	1.65	1.90	0.62	1.75

submitted copy

D3*	2.12	2.23	3.14	1.62
E3*	0.58	0.73	0.47	0.46
F3*	1.66	1.48	3.15	1.49
G3	1.39	1.54	0.58	1.43
F4*	1.19	2.26	3.19	1.49

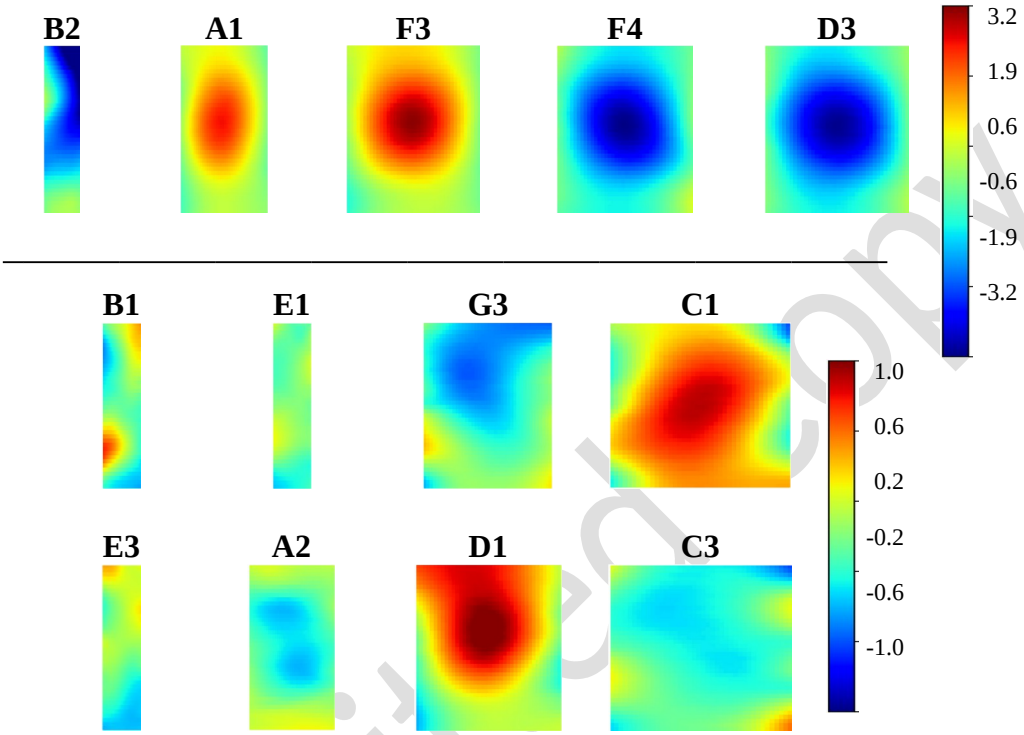


Figure 4. Interpolated surface visualization of web geometric imperfections.

5. Stub Column Test Procedure

The thirteen stub column tests were completed using an Instron 8804MT press and load cell with 600kN static load capacity. The load was applied in displacement control at a rate of 0.2mm/s, allowing the investigation of post-ultimate strength behaviour. The use of rates between 0.1-0.3mm/min is customary in studies for quasi-static steel compression tests [39, 40, 41, 17, 42]. The Instron press measured the end-shortening of the column. Strains were measured in one of the flanges at mid-height by the VE with measurement accuracy of ±0.5%. The VE measured the distance between two points drawn on the flange and compared them to the measurement before loading to compute strains. Finally, a strain field on the entire web was measured using digital image correlation (DIC). Two Allied Vision

Submitted copy

Technologies cameras were fitted with 25mm focal length Kowa lenses and set up in stereo configuration at 1300mm from the stub column, facing the web. The images produced have resolution of 4122 by 2176 pixels. Prior to testing, the specimens were spray-painted in matt white with a black speckle pattern on the web for DIC measurement. The minimum target size of the black speckles based on the camera resolution and the distance to the object was 0.54mm. A full diagram of the test setup is shown in Figure 5.

The stub columns were geometrically centred on the loading press and put into contact with both the loading and support platens. The original contact locations of the column with the platens were marked. Before loading, a detailed diagram of the column contacts with both platens was created to quantify the deviations from an assumption of perfectly uniform contact. After the calibration of DIC and VE cameras, a pre-load of 3kN was established before balancing the actuator. The critical assumption of fixed-fixed end conditions held true beyond the ultimate strength for all specimens – verified as the columns did not slip from the original contact locations marked on the platen.

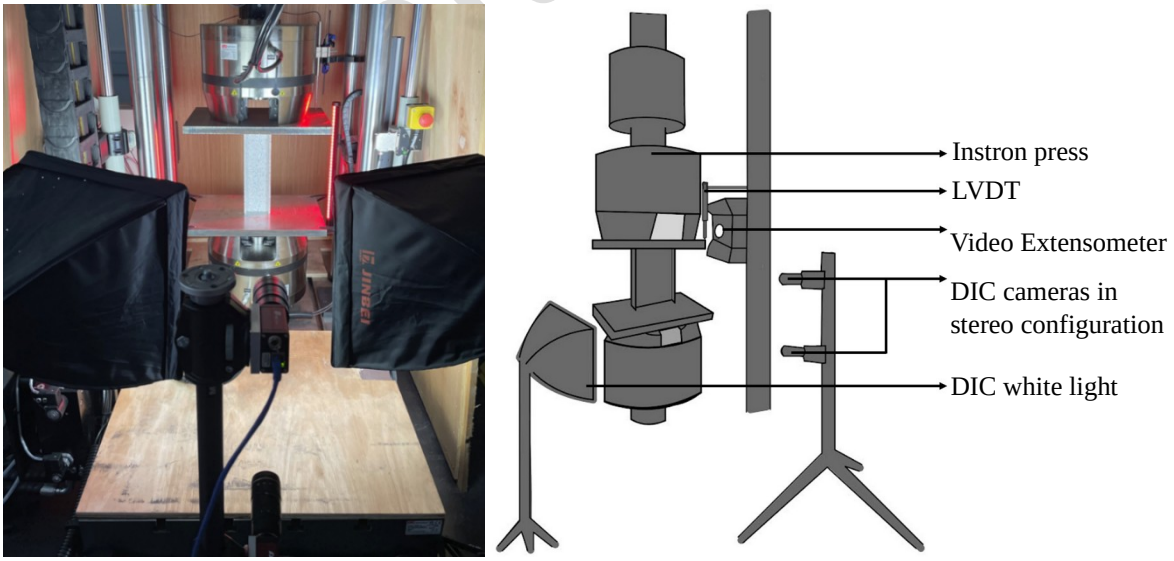


Figure 5. Photo and diagram of stub column experimental set-up.

6. Tests and Numerical Validation

Submitted Copy

All stub columns were compressed beyond the point of their ultimate strength. Among the thirteen stub columns, one failed with local-global interaction buckling, and the remaining twelve underwent local buckling with substantial flange resistance followed by local plastification. The variation in the local buckling mechanisms is primarily influenced by differences in the geometry or materials of the plates.

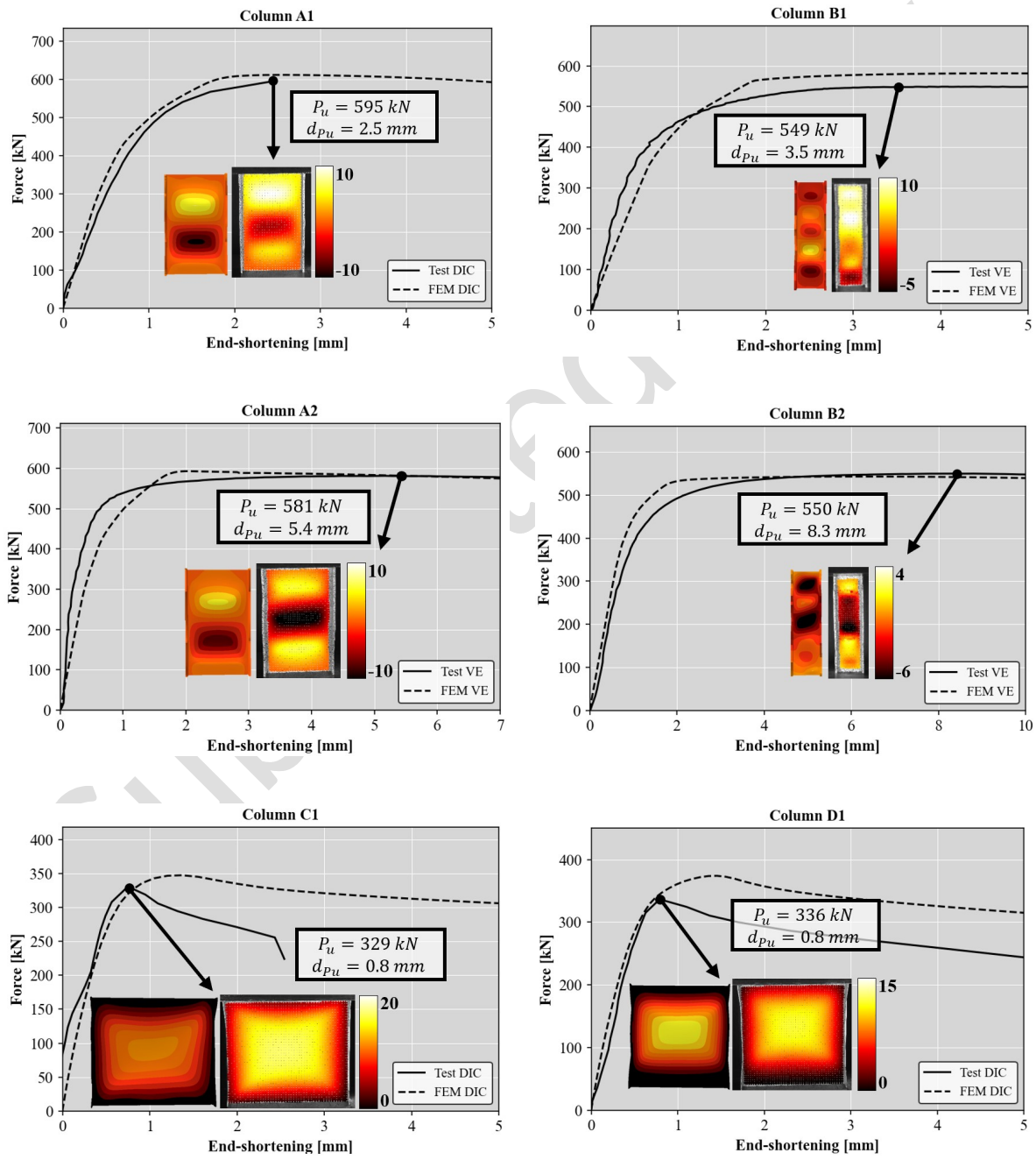
6.1. Test Results

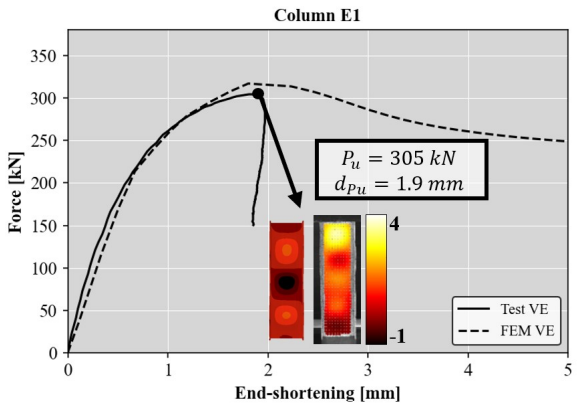
The force-displacement curves for all thirteen stub column tests are reported in Figure 6. Force measurements were taken from the Instron press data. End shortening is measured by two methods. First, strain readings taken by the VE from the mid-length of the flange and scaled it up to the full length of the column estimate the end-shortening. The VE has the advantage of eliminating errors from the load string compliance, but this method to calculate end-shortening assumes a perfectly uniform distribution of stresses and, since it is measuring along a line parallel to the flange, is inaccurate if there is any non-axial motion in the flanges. DIC also measured end-shortening, but the image data is sensitive to small changes in lighting (sunlight), surrounding temperature (localised heat), and inaccurate once (if) the paint chips or flakes. Therefore, engineering judgment was applied to determine which of these two measurements most accurately capture the behaviours of interest, as indicated in the legends of Figure 6. Both the VE and DIC readings are more reliable before reaching the ultimate force as flange rotations and paint chipping generally begin after that point.

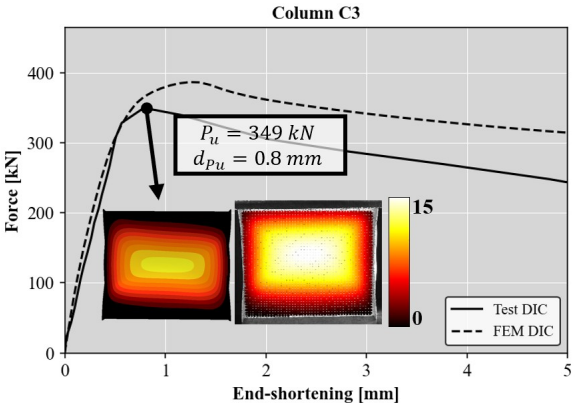
The plots in Figure 6 also include the force-displacement curves from the FE model corresponding directly to the end shortening measurement method used for that column, which will be discussed further in Section 6.3. The ultimate load sustained by the columns and the measured level of end-shortening at this point are labelled. Finally, graphics of the column FE model (left) and DIC measurements (right) at the point of ultimate force are provided within the graph for each column. The colour gradient corresponds to the measured

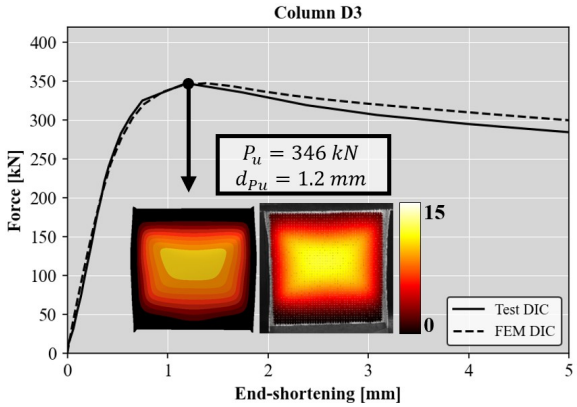
Submitted Copy

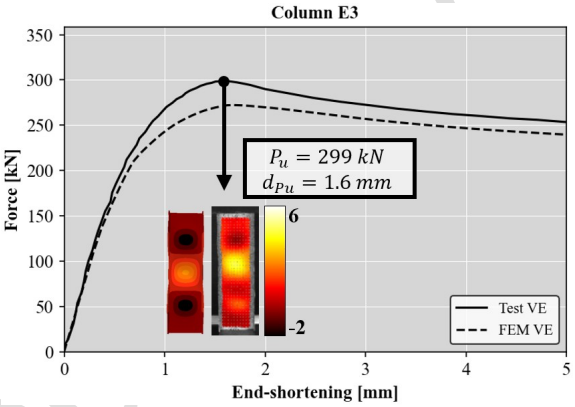
out-of-plane displacements to visualize the buckling shape and deformation magnitudes at ultimate force. Equivalent colour scales are used to enable direct comparison between the FE model prediction and DIC measurements.

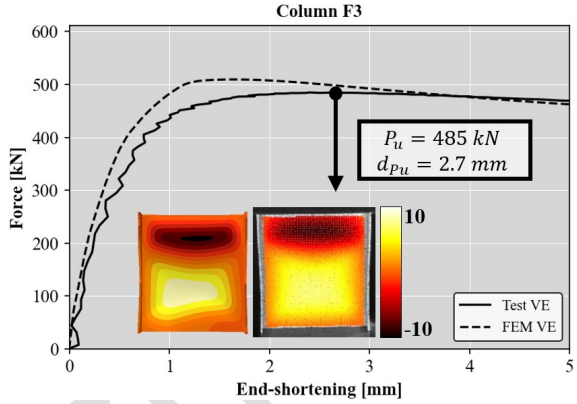


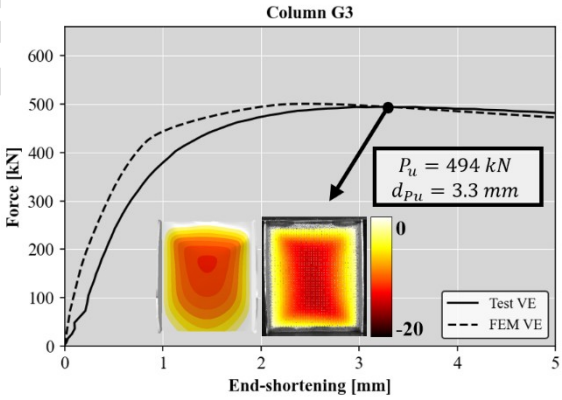

Column E1
$P_u = 305\ kN$
$d_{Pu} = 1.9\ mm$
4
-1
Test VE
FEM VE
Force [kN]
End-shortening [mm]


Column C3
$P_u = 349\ kN$
$d_{Pu} = 0.8\ mm$
15
0
Test DIC
FEM DIC
Force [kN]
End-shortening [mm]


Column D3
$P_u = 346\ kN$
$d_{Pu} = 1.2\ mm$
15
0
Test DIC
FEM DIC
Force [kN]
End-shortening [mm]


Column E3
$P_u = 299\ kN$
$d_{Pu} = 1.6\ mm$
6
-2
Test VE
FEM VE
Force [kN]
End-shortening [mm]


Column F3
$P_u = 485\ kN$
$d_{Pu} = 2.7\ mm$
10
-10
Test VE
FEM VE
Force [kN]
End-shortening [mm]


Column G3
$P_u = 494\ kN$
$d_{Pu} = 3.3\ mm$
0
-20
Test VE
FEM VE
Force [kN]
End-shortening [mm]

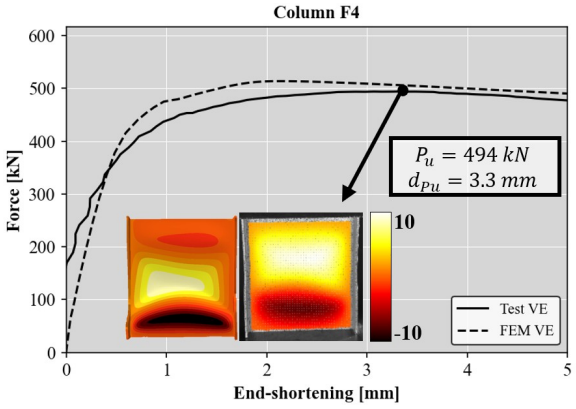

Column F4
$P_u = 494\ kN$
$d_{Pu} = 3.3\ mm$
10
-10
Test VE
FEM VE
Force [kN]
End-shortening [mm]

Figure 6. Force-displacement curves from stub column tests and FE models. Graphics within each plot show FE model results (left) and DIC measurements (right) for out-of-plane deformations in millimetres at the point of ultimate force. P_u is the ultimate force supported by the column and d_{Pu} is the end-shortening value at the point of ultimate force.

6.2. Buckling Mechanisms

All stub columns initially locally buckled in the web. Localized flange rotations developed, generally occurring after the point of ultimate force, in sections with large web deformations (i.e. C1, D1, E1, C3, D3, E3, and F3) to accommodate the increasingly deformed shape. This observation supports the hypothesis that when I-profile flanges are substantially stronger than the web plate (strong flange), the web may locally buckle with minimal flange deformation and the section ultimate strength can be approximated as the sum of the web plate local buckling capacity and the flange fully plastic capacity [32]. The number of buckling half waves developed in each column was primarily determined by the aspect ratio of the web plate, consistent with Timoshenko & Gere's description of plate buckling [43]. Variations to the theoretical web buckling shape were observed, however, due to influences including the column initial imperfections and imperfect initial contact between the column and platens.

Figure 7 shows the deformed shape of all stub columns after the compression tests. FE model results at equivalent levels of end-shortening are included in Figure 7 with the colour gradient representing the out-of-plane deformations in millimetres.

The influence of flange strength on buckling behaviour is most clearly demonstrated by the differences between columns B1, E1, and E3. First, column B1 is the only specimen to exhibit local-global interaction buckling. It developed five local buckling half-waves in the web – each with small out-of-plane deformation. This was caused by the B1 flanges (6mm thick of 1.4462) providing substantial resistance, resembling fixed-fixed end conditions on the web buckling mode. This is contrasted with column E1 – which has identical materials

Submitted copy

417 and only thinner flanges, 3mm, than B1 – where the flanges provide less resistance. In
418 column E1, three buckling half-waves formed, the middle half-wave characterised by large
419 out-of-plane deformations, and eventually the flanges rotate at the location of the web buckle
420 to accommodate the deformation. Column E3 – which has identical geometry as E1 but a
421 slightly weaker 1.4404 web – exhibited the same buckling mechanism as column E1. The
422 reduction in web strength was not substantial enough to affect the buckling shape.

423 The comparison of columns A1 and B1 (1.4307 in the web) to A2 and B2 (S275 in the
424 web) isolates the change in web material from stainless steel to carbon steel. The measured
425 proof strength $\sigma_{0.2}$ of carbon steel grade S275 is approximately 20% greater than that of
426 stainless steel grade 1.4307. This difference, expectedly, did not substantially change the
427 observed buckling behaviour and did not increase the ultimate strength of the sections with
428 carbon steel webs. In the logic of the EWM, the buckling strength of the carbon steel webs is
429 reduced because they have larger f_y than the 1.4307 stainless steel, leading to smaller values
430 of the material factor ε, and therefore more slender classifications – or smaller reduction
431 factors ρ. A1 and A2 both have Class 4 webs, but the reduction factor ρ is smaller for A2.
432 Section B1's web is Class 2, while section B2's web is Class 3. Columns A2 and B2 are not
433 able to make efficient use of the greater material strength in their web because their increased
434 f_y leads to instability.

435 The comparison of columns C1 to D1 (1.4307 in the web) and C3 to D3 (1.4404 in the
436 web) isolates the effect of web height reduction. These four columns exhibit very similar
437 buckling shapes. The effect of the web height on ultimate force is small in these columns and
438 overshadowed by other factors including initial imperfections. It is clear, however, that D1
439 and D3 are more efficient than C1 and C3 as they achieve similar ultimate strengths despite
440 having smaller cross-sectional areas.

Submitted Copy

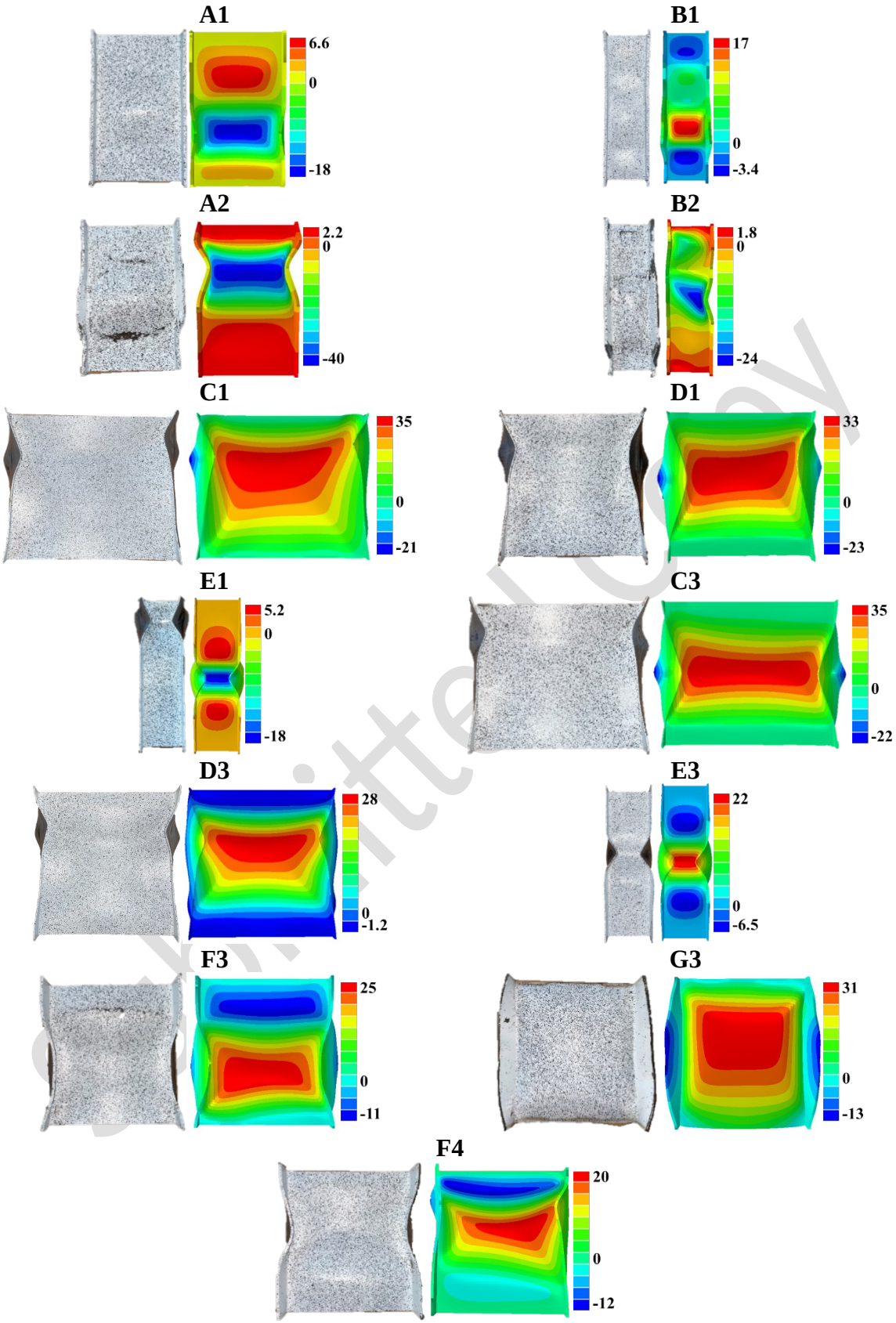


Figure 7. Comparison of stub column deformed shape with FE model results. Colour scale of FE model represents the out-of-plane displacements in millimetres.

Relative to column D3, F4 has a smaller web height h_w, smaller width-to-thickness ratio in the flange plates, and a much lower material strength in the flange – all of which make the plates in this section less susceptible to local buckling. As expected, the lower slenderness of F4 caused it to locally buckle at higher forces. Column D3 achieved an ultimate strength that is 62% of its fully plastic capacity while column F4 achieved 78%, as seen in Figure 8. F3 and G3 – which both have the increased flange thickness of 6mm, like F4 – reached ultimate strengths that were 80% and 83%, respectively, of their fully plastic capacity.

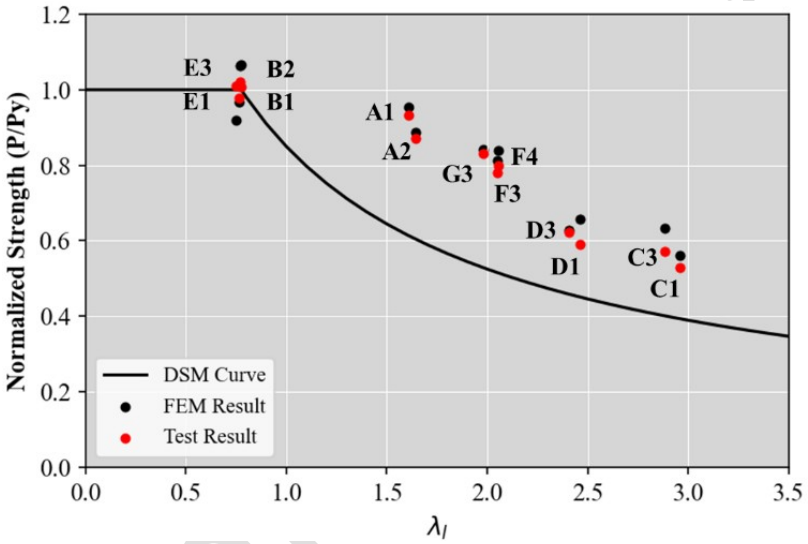


Figure 8. Normalized strength vs. slenderness for stub column tests and FE model results.

In Figure 8, the normalised strength of each section – the observed ultimate strength divided by the fully plastic strength P_y, defined as $(2f_{y,f}t_f b)+(f_{y,w}t_w h_w)$ – is plotted against the sectional slenderness λ_l, defined as $\sqrt{P_{ne}/P_{crl}}$. The observation that the stub column test results are plotted above the DSM curve is evidence of strong flange behaviour – the tendency for sections with sufficiently strong flanges to exhibit higher ultimate strengths than existing design methods account for.

6.3. Numerical Modelling and Validation

Submitted

Finite element models were developed using Abaqus Standard [44] explicit solution procedure to numerically represent the stub column compression experiments and investigate the sensitivity of ultimate capacity to primary parameters such as geometric imperfection, weld geometry and residual stress model. The stub columns were modelled using 4-node shell elements with reduced integration (S4R), which have been repeatedly shown successful for this type of model [20, 45, 16, 19]. The loading and bearing plates were modelled as non-deforming rigid 4-node quadrilateral elements (R3D4). All degrees of freedom (DOF) were locked on the bottom bearing plate (no motion). The upper loading plate had all DOF locked except for motion along the loading axis (free *z*-axis translation). At locations where the column was measured to be in-contact with the plates, a fixed connection is represented by giving the column ends and the platen coinciding nodes.

A mesh convergence study was conducted to appropriately trade-off result precision against computational time. The selected mesh density is a 5mm square mesh throughout the stub column and 15mm mesh in the bearing and loading plates. The fillet weld connecting the web and flange plates is not represented with any additional elements. Representation of the weld was removed because the overlapping area of elements in the web and flange accounted for areas approximately equal to the area of the fillet weld. Additionally, the effect of the weld representation was found to be small relative to other parameters in a sensitivity assessment.

The nominal length of all specimens was set to 350 mm to ensure full development of local buckling in each specimen. The dimensions of specimens in Abaqus were defined consistently with the diagram in Figure 1 and used the measured values reported in Table 3. In general, the homogeneous specimens were designed with webs having a significantly higher width-to-thickness ratio compared to the flanges to ensure that strong flange behaviour would be observed in all the cross-sections. A schematic of the FE model is given in Figure 9.

Submitted Copy

The stub column test model applied static point loading in increments using the static RIKS method [44].

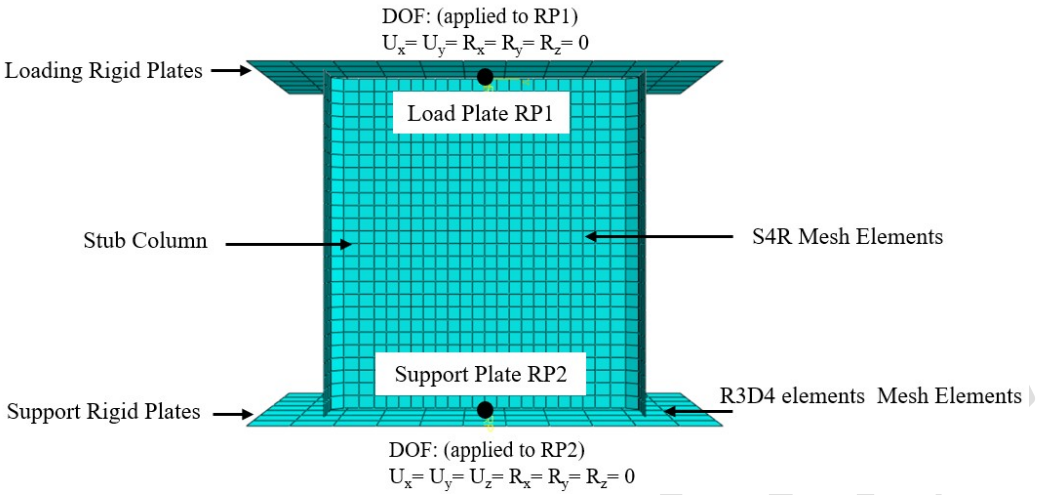


Figure 9. Schematic of the stub column test FE model.

The material constitutive models for stainless steel were defined by the two-stage Ramberg-Osgood model specified in the Design Manual for Stainless Steel [46]. Carbon steel material was modelled as elastic-perfectly-plastic. The model parameters for E, f_y, and f_u were taken from the measured values reported in Section 3. All other parameters in the model were defined using the equations provided in the codes.

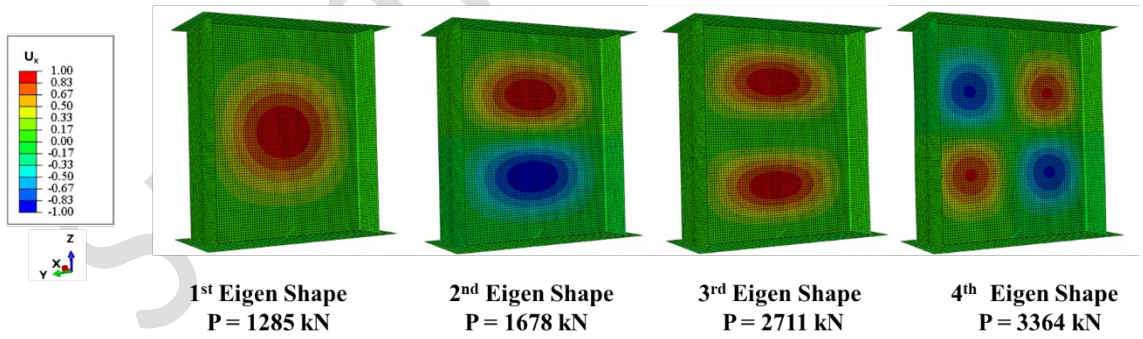


Figure 10. First four eigenmodes of a stub column under linear buckling analysis.

To determine the shape of geometric imperfections, a linear buckling analysis was performed for each section using a linear perturbation step with a unit load applied at the reference point on the top rigid plate to extract the buckling mode shapes [19, 47]. The first four eigenmodes were obtained for each section, as shown in Figure 10 for a representative

section. The first eigenmode always corresponds to the lowest elastic buckling load. The nodal coordinates associated with the first eigen shape were saved and subsequently imported into the nonlinear static analysis. The spatial distribution of imperfections in the model thus followed the first buckling mode shape. Following a procedure successfully applied in numerous other studies on steel columns [42, 48, 19, 20], that shape was scaled up, setting the maximum imperfection among the plates in each section equal to the imperfection factor measured for that specimen,determined in Section 4, Table 5.

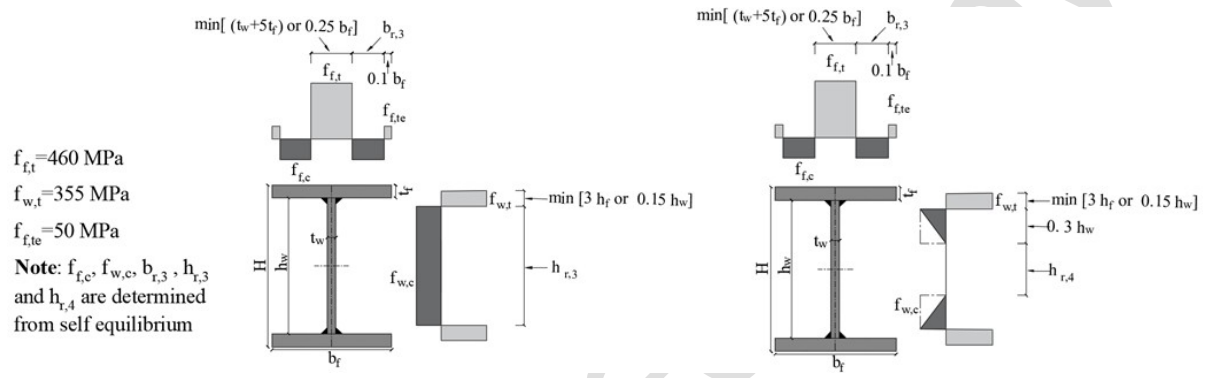


Figure 11. Residual stress profile from [24] used in FE models. Profile (a) is used when $h_w \leq$ 210mm, and profile (b) is used when $h_w >$ 210mm.

Residual stresses induced by welding and uneven cooling also contribute to premature yielding and a reduction in structural stiffness [49]. The longitudinal residual stresses were modelled as equilibrium rectangular and triangular block stress distributions, with magnitudes obtained from [24] based on the profile originally developed by [50]. The triangular distribution in the web is applied here as it was developed to represent sections with tall webs (>210mm) [50], which is the more likely use case for hybrid stainless steel I-sections. The stresses are tensile (positive) at the junction of the web and flange and compressive (negative) elsewhere, such that the tensile and compressive residual stresses are in self-equilibrium within each plate. This residual stress model [24] was selected primarily because it was developed specifically for (welded) hybrid I-sections. Although originally developed for high-strength steel, the model from [24] is adopted here for stainless steel due

Submitted

to the similarities in their mechanical responses, i.e., both materials exhibit pronounced nonlinearity and high yield strength. The validity of this approach is further supported by a sensitivity analysis to a second residual stress model [51], which showed negligible variation in the strength predictions. Figure 11 shows the profile of the residual stresses, including the distribution and magnitude of stresses used in the numerical model, with all parameter magnitudes given in Figure 11 determined per the method using in [24, 50].

A mesh refinement study was conducted for the S4R elements comprising the stub columns, as presented in Table 6, to find a balance between accuracy and computational cost which will inform the future application of this model to in parametric studies. Two sections made of EN 1.4062, with distinct buckling behaviour were selected for mesh sensitivity study. The ultimate strength P_u and end-shortening δ calculated by the FE model for both sample columns is reported for ten potential mesh sizes. The 5 × 5mm mesh size was selected for the S4R elements.

Table 6. Mesh sensitivity analysis.

Model No.	**S4R Mesh Size**	$h_w \times b_f \times t_f \times t_w$ $170 \times 80 \times 6 \times 4$		$h_w \times b_f \times t_f \times t_w$ $470 \times 80 \times 6 \times 4$	
	mm	P_u	δ	P_u	δ
1	20 × 20	901.78	0.95	976.96	2.42
2	15 × 15	896.62	0.96	976.08	2.37
3	12 × 12	893.44	0.92	972.26	2.37
4	10 × 10	893.03	0.92	971.40	2.36
5	8 × 8	891.36	0.91	970.09	2.37
7	7 × 7	891.13	0.93	969.63	2.36
6	6 × 6	890.57	0.92	969.18	2.36
8	5 × 5	890.19	0.93	968.77	2.37
9	4 × 4	889.59	0.93	967.99	2.37
10	3 × 3	889.23	0.92	967.64	2.37

Ultimate strength values from the FE models are compared against the test results in Table 7 and show generally strong agreement. The alignment of the force-displacement curves from the FE model and test results in Figure 6 and the accurate representation of

Submitted Copy

deformed shapes in Figure 7 also demonstrate that the FE model is capturing the relevant characteristics of the tested stub columns.

Table 7. Comparison of ultimate loads from tests and numerical results.

Specimen	$P_{u,test}$ [kN]	$P_{u,FE}$ [kN]	$P_{u,test} / P_{u,FE}$
A1	595*	611	0.98
B1	549	582	0.94
A2	581	593	0.98
B2	550	543	1.01
C1	329	349	0.94
D1	336	375	0.90
E1	305	317	0.96
C3	349	387	0.90
D3	346	349	0.99
E3	299	272	1.10
F3	485	510	0.95
G3	494	501	0.99
F4	494	514	0.96
Average			**0.97**
S.D.			**0.05**

* Test A1 was terminated at 595 kN to prevent exceeding the press capacity. If the test ran to completion, it is estimated that the ultimate force would be an additional 1%.

The FE model provides the opportunity to investigate which specific parameters in each column are influencing ultimate strength and buckling behaviour. The FE model was built incrementally to individually introduce new parameters and observe their effects. As expected, incorporation of geometric imperfections of the measured magnitudes resulted in a substantial decrease in the predicted ultimate strength. Addition of the initial residual stresses slightly reduced the ultimate strength and caused an earlier departure from linearity in the force-displacement curve. A parametric assessment of the material model parameters found that ultimate strength was much more sensitive to f_y than f_u or n, the non-linearity parameter for stainless steel. These relationships were expected and well covered in previous literature.

The FE model also proved to be sensitive to the representation of initial contact imperfections. In the test setup, it was observed that small gaps (<1mm) between the column

Submitted copy

554 and the platens were present at some locations. Measurements of the size and location of
555 these gaps were made before running the test. Contact imperfections were represented in the
556 FE model by de-coupling nodes in the platen and column, which were otherwise defined as
557 coinciding to represent a perfectly fixed end condition. Incorporation of the measured
558 asymmetrical contact imperfections resulted in reductions to the ultimate strength and
559 allowed for the accurate representation of asymmetrical buckling development, as seen in
560 columns C1 and D1.

561 **7. Conclusions**

562 This study conducted tests to understand the fundamental loading case of compression
563 for hybrid I-sections which, in application, are often designed with strong flanges. Thirteen
564 stub columns were tested to investigate the effect of hybridity and geometrical proportions on
565 compression behaviour. The tests also provide the first experimental evidence of stainless-
566 steel hybrid I-profile behaviour, with or without strong flanges.

567 The stub column tests provide substantial evidence that I-sections characterised by
568 strong flanges exhibit distinctly different behaviour from conventional, more uniformly
569 proportioned sections. Interaction between the capacity of the flanges and the web buckling
570 mode is demonstrated by controlled experiments changing the flange thickness between
571 sections. Sections with greater flange thickness also generally exhibited greater structural
572 efficiency. Critically, sections with increased flange strength developed ultimate strengths
573 much greater than the predictions from existing design methods. Geometry proved to have a
574 greater effect on local buckling behaviour than material properties – which is consistent with
575 the existing equations for section slenderness classification. High strength materials are not
576 efficiently employed when the greater material strength leads to local buckling strength
577 reductions driven by the increase of slenderness. Stub column ultimate strength and buckling
578 behaviour is accurately reflected in a validated FE model. Agreement between experimental

Submitted Copy

results and the numerical model strengthens the findings in Section 6 about the effect of material, geometric, and initial imperfection parameters on stiffness and ultimate strength.

Among the tested columns, the observed ultimate strengths normalized by fully plastic strength achieved by hybrid sections was negligibly different from homogenous sections when controlling for sectional slenderness λ_l. Further, columns in this study with hybrid ratios up to 2.29 showed no indications of reduced structural efficiency. This provides standing to assume that the optimal hybrid ratio of 1.3-1.6 recommended by Terreros-Bedoya et al. [2] for flexural members (to achieve post-critical resistances that maximize the web's capacity) should be replaced for hybrid compression members by a different – more complete – ratio encompassing thickness and yield strength for both the web and the flanges to distinguish between behaviours and more adequately evaluate member efficiency.

In a companion paper, the authors use the validated FE model to generate evidence of strong flange behaviour for a complete range of material and geometric possibilities [34]. That research, developed using the experimental results in this paper, concludes by providing a modified DSM formulation which is sufficient to design for strong flange behaviour of I-sections. It accounts for the different effective strengths in each plate without sacrificing too much of the original method's simplicity by incorporating only two additional parameters which are calculated as simple ratios of geometrical dimensions.

Data Availability Statement

All data, models, and code generated or used during the study appear in the submitted article.

Acknowledgements

The fabrication of experimental specimen for this research was done by Whittaker Engineering of Stonehaven, UK. They were excellent partners in manufacturing and the communication of technical information. Gregory Langone is an Engineer Officer in the U.S.

Submitted Copy

Army and a recipient of the John & Daria Barry Scholarship which generously supports his studies. Usman Ali is a doctoral candidate whose research and studies are funded by the Marie Skłodowska-Curie Doctoral Network (MSCA-DN) SeaChem project, EU Grant No. 101073471. Majid Shamlooei (majid.shamlooei@unitn.it) contributed to the preliminary development of the finite element model.

References

[1] F. Javidan, A. Heidarpour, X.-L. Zhao and J. Minkkinen, "Application of high strength and ultra-high strength steel tubes in long hybrid compressive members: Experimental and numerical investigation," *Thin-Walled Structures,* vol. 102, pp. 273-285, May 2016.

[2] A. Terreros-Bedoya, I. Negrin, I. Paya-Zaforteza and V. Yepes, "Hybrid steel girders: Review, advantages and new horizons in research and applications," *Journal of Constructional Steel Research,* vol. 207, 2023.

[3] American Association of State Highway and Transportation Officials, AASHTO LRFD Bridge Design Specificiations, 4th Edition ed., Washington DC, 2007, pp. 6.84-6.85.

[4] CEN (Committee of European Normalization), Eurocode 3: Design of steel structures - Part 1-5: General rules - Plated structural elements. (EN 1993-1-5), Brussels, 2006.

[5] R. Frost and C. Schilling, "Behavior of Hybrid Beams Subjected to Static Loads," *Journal of the Structural Division ASCE,* vol. 90, no. 3, June 1964.

[6] Joint American Society of Civil Engineers-AAHSO Committee, "Design of Hybrid Steel Beams," *Journal of the Structural Division ASCE,* vol. 94, no. 6, June 1968.

[7] J. Mozer, R. Ohlson and C. Culver, "Horizontally curved highway bridges: Stability of curved plate girders," 1971.

[8] M. Veljkovic and B. Johansson, "Design of hybrid steel girders," *Journal of Constructional Steel Research,* vol. 60, no. 3-5, pp. 535-547, 2004.

[9] J.-z. Liu, S. Chen and T.-M. Chan, "Experimental and numerical investigations of hybrid high strength steel welded T-section stub columns with Q690 flange and Q460 web," *Thin-Walled Structures,* vol. 177, 2022.

[10] N. R. Nagaraja Rao, P. Marek and L. Tall, "Hybrid steel columns, May 1969 (72-37)," Fritz Laboratory Reports, 1969.

[11] N. R. Nagaraja Roa, P. Marek and L. Tall, "Welded hybrid steel columns," *Welding Journal Research Supplement,* pp. 462-472, September 1972.

[12] X.-L. Zhao, D. V. Binh, R. Al-Mahaidi and Z. Tao, "Stub column tests of fabricated square and triangular sections utilizing very high strength steel tubes," *Journal of Constructional Steel Research,* vol. 60, no. 11, pp. 1637-1661, November 2004.

[13] D. V. Binh, B. Al-Mahaidi and X.-L. Zhao, "Finite Element Analysis (FEA) of Fabricated Square and Triangular Section Stub Columns Utilizing Very High Strength Steel Tubes," *Advances in Structural Engineering,* vol. 7, no. 5, 2004.

[14] J. Rhodes, X.-L. Zhao, B. V. Binh and R. Al-Mahaidi, "Rational design analysis of stub columns fabricated using very high strength circular steel tubes," *Thin-Walled Structures,* vol. 43, no. 3, pp. 445-460, March 2005.

[15] M. A. Farmani, A. Heidarpour and C. Woo, "Thermal creep of hybrid steel columns comprising ultra-high strength steel tubes and stainless steel plates under transient fire

Submitted Copy

conditions," *Thin-Walled Structures,* vol. 185, 2023.
[16] R. Lalthazuala and K. Singh, "Structural behaviour of hybrid stainless steel stub columns under axial compression," *Structures,* vol. 27, pp. 128-140, October 2020.
[17] J.-z. Liu, S. Chen and T.-M. Chan, "Testing, numerical modelling and design of Q690 high strength steel welded T-section stub columns," *Engineering Structures,* vol. 259, May 2022.
[18] S. Chen, J.-z. Liu and T.-M. Chan, "Investigations into the local buckling and post-buckling behaviour of fixed-ended hybrid I-section stub columns with slender web," *Thin-Walled Structures,* vol. 184, 2023.
[19] S. Chen, J.-z. Liu and T.-M. Chan, "Local buckling behaviour of high strength steel and hybrid I-sections under axial compression: Numerical modelling and design," *Thin-Walled Structures,* vol. 191, October 2023.
[20] M. Bock, M. Gkantou, M. Theofanous, S. Afshan and H. Yuan, "Ultimate behaviour of hybrid stainless steel cross-sections," *Journal of Constructional Steel Research,* vol. 210, November 2023.
[21] N. R. Nagaraja Rao, The strength of hybrid steel columns, Lehigh University, Ph.D., 1965.
[22] T. Aoki and B. Ji, "Experimental study on buckling strength of tri-tube steel members," in *Proceeding of the Third International Conference on Coupled Instabilities in Metal Structures*, Lisbon, Portugal, 2000.
[23] M. A. Farmani, A. Heidarpour and X.-L. Zhao, "Thermal creep of austenitic stainless steel plate material under transient heating conditions," *Thin-Walled Structures,* vol. 171, February 2022.
[24] S. Chen, J.-z. Liu and T.-M. Chan, "Material properties and residual stresses of welded high strength steel and hybrid I-sections," *Engineering Structures,* vol. 276, February 2023.
[25] B. Rossi, "Discussion of the use of stainless steel in construction in view of sustainability," *Thin-Walled Structures,* vol. 83, pp. 182-189, October 2014.
[26] B. Karabulut, G. Ferraz and B. Rossi, "Lifecycle cost assessment of high strength carbon and stainless steel girder bridges," *Journal of Environmental Management,* vol. 277, January 2021.
[27] L. Gardner, "The use of stainless steel in structures," *Progress in Structural Engineering and Materials,* vol. 7, 21 February 2005.
[28] G. van den Berg, "The effect of the non-linear stress–strain behaviour of stainless steels on member capacity," *Journal of Constructional Steel Research,* vol. 54, no. 1, pp. 135-160, April 2000.
[29] H. Yuan, Y. Wang, L. Gardner, X. Du and Y. Shi, "Local–overall interactive buckling behaviour of welded stainless steel I-section columns," *Journal of Constructional Steel Research,* vol. 111, pp. 75-87, 2015.
[30] H. Ran, Z. Chen and Y. Ma, "Experimental and numerical studies of laser-welded slender stainless steel I-section columns," *Thin-Walled Structures,* vol. 171, 2022.
[31] L. Gardner, Y. Bu and M. Theofanous, "Laser-welded stainless steel I-sections: Residual stress measurements and column buckling tests," *Engineering Structures,* vol. 127, pp. 536-548, November 2016.
[32] B. Rossi and Y. Li, "Extension of the DSM to welded H profile cross-sections," in *Research and Applications in Structural Engineering, Mechanics and Computation*, 2013, pp. 1291-1296.
[33] G. Langone, M. Shamlooei, U. Ali, X. Ruan and B. Rossi, "Extension of the direct

Submitted Copy

strength method to fabricated I-profiles under compression," in *Nordic Steel Construction Conference*, Lulea, Sweeden, 2024.

[34] U. Ali, G. Langone and B. Rossi, "Design of stainless steel homogeneous and hybrid I-sections exhibiting strong flange behaviour," *ASCE Journal of Structural Engineering,* 2025.

[35] M. Seif and B. W. Schafer, "Local buckling of structural steel shapes," *Journal of Constructional Steel Research,* vol. 66, no. 10, pp. 1232-1247, October 2010.

[36] G. H. Bryan, "On the Stability of a Plane Plate under Thrusts in its own Plane, with Applications to the "Buckling" of the Sides of a Ship," *Proceedings of the London Mathematical Society,* Vols. s1-22, no. 1, pp. 54-67, 01 November 1890.

[37] International Organization for Standardization, "ISO 6892-1: Metallic materials - Tensile testing. Part 1: Method of test at room temperature," 2019-11.

[38] K. Tseng and C. Chou, "Effect of pulsed gas tungsten arc welding on angular distortion in austenitic stainless steel weldments," *Science and Technology of Welding and Joining,* vol. 6, no. 3, pp. 149-153, 2001.

[39] J.-H. Zhang and B. Young, "Compression tests of cold-formed steel I-shaped open sections with edge and web stiffeners," *Thin-Walled Structures,* vol. 52, pp. 1-11, March 2012.

[40] H. Fang, T.-M. Chan and B. Young, "Behavior of Octagonal High-Strength Steel Tubular Stub Columns," *Journal of Structural Engineering,* vol. 145, no. 12, 2019.

[41] Y. Sun, Y. Liang and O. Zhao, "Testing, numerical modelling and design of S690 high strength steel welded I-section stub columns," *Journal of Constructional Steel Research,* vol. 159, pp. 521-533, August 2019.

[42] K. Jiang and O. Zhao, "Stainless steel built-up section stub columns: Testing, numerical modelling and design," *Thin-Walled Structures,* vol. 191, October 2023.

[43] S. Timoshenko and J. Gere, Theory of Elastic Stability, 2nd ed., New York: McGraw-Hill Book Company, 1961.

[44] Dassault Systems Simulis Corp, "ABAQUS/CAE User's Manual," Providence, RI, 2022.

[45] M. Theofanous and L. Gardner, "Experimental and numerical studies of lean duplex stainless steel beams," *Journal of Constructional Steel Research,* vol. 66, no. 6, pp. 816-825, June 2010.

[46] SCI (Steel Construction Institute), "Design Manual for Structural Stainless Steel, 4th Edition," SCI, Berkshire, 2017.

[47] N. Saliba and L. Gardner, "Cross-section stability of lean duplex stainless steel welded I-sections," *Journal of Constructional Steel Research,* vol. 80, pp. 1-14, January 2013.

[48] H. X. Yuan, Y. Wang, Y. Shi and L. Gardern, "Stub column tests on stainless steel built-up sections," *Thin-Walled Structures,* vol. 83, pp. 103-114, October 2014.

[49] M. Abambres and W.-M. Quach, "Residual stresses in steel members: a review of available analytical expressions," *International Journal of Structural Integrity,* vol. 7, no. 1, pp. 70-94, February 2016.

[50] H. Y. Ban, "Research on the overall buckling behavior and design method of high strength steel columns under axial compression," Tsinghua University, Beijing, 2012.

[51] H. Yuan, Y. Wang, Y. Shi and L. Gardner, "Residual stress distributions in welded stainless steel sections," *Thin-Walled Structures,* vol. 79, pp. 38-51, June 2014.

610
611

Submitted copy